

DMAligner: Enhancing Image Alignment via Diffusion Model Based View Synthesis

Xinglong Luo¹, Ao Luo², Zhengning Wang^{1†},

Yueqi Yang, Chaoyu Feng, Lei Lei, Bing Zeng¹, and Shuaicheng Liu^{1†}

¹University of Electronic Science and Technology of China ²Southwest Jiaotong University

{xinglong.luo@std., zhengning.wang@, liushuaicheng@}uestc.edu.cn aoluo@swjtu.edu.cn

Abstract

Image alignment is a fundamental task in computer vision with broad applications. Existing methods predominantly employ optical flow-based image warping. However, this technique is susceptible to common challenges such as occlusions and illumination variations, leading to degraded alignment visual quality and compromised accuracy in downstream tasks. In this paper, we present DMAligner, a diffusion-based framework for image alignment through alignment-oriented view synthesis. DMAligner is crafted to tackle the challenges in image alignment from a new perspective, employing a generation-based solution that showcases strong capabilities and avoids the problems associated with flow-based image warping. Specifically, we propose a Dynamics-aware Diffusion Training approach for learning conditional image generation, synthesizing a novel view for image alignment. This incorporates a Dynamics-aware Mask Producing (DMP) module to adaptively distinguish dynamic foreground regions from static backgrounds, enabling the diffusion model to more effectively handle challenges that classical methods struggle to solve. Furthermore, we develop the Dynamic Scene Image Alignment (DSIA) dataset using Blender, which includes 1,033 indoor and outdoor scenes with over 30K image pairs tailored for image alignment. Extensive experimental results demonstrate the superiority of the proposed approach on DSIA benchmarks, as well as on a series of widely-used video datasets for qualitative comparisons. Our code is available at <https://github.com/boomluo02/DMAligner>.

1. Introduction

The alignment of consecutive frames is a critical task in computer vision, supporting a wide range of applications such as High Dynamic Range (HDR) imaging [6, 8, 53],

[†] Corresponding Author.

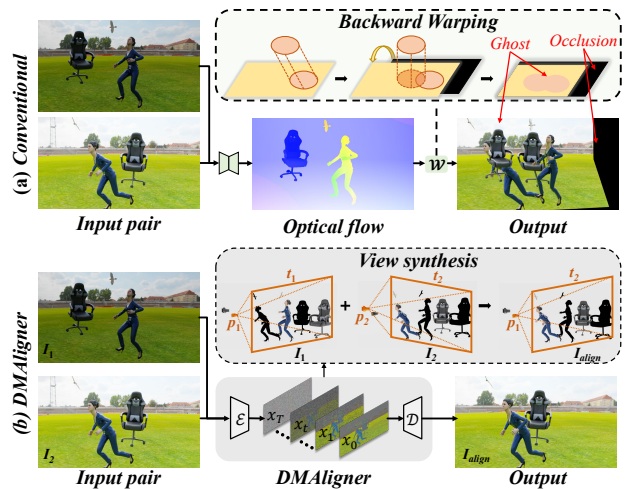


Figure 1. (a) Conventional image alignment based on optical flow and image warping, resulting in ghosting artifacts and occlusion. (b) Our DMAligner directly generate the complete alignment image via diffusion-based view synthesis.

video stabilization [26], image deblurring [58], and super-resolution [5]. Precise alignment ensures the accurate merging of information from consecutive frames, leading to enhanced image quality and better performance in subsequent tasks [37, 51, 52]. Despite its significance, the task of image alignment remains challenging due to various factors, including scene dynamics, large camera motion, and varying lighting conditions.

Recent advancements in deep learning have led to substantial progress in neural network-based alignment methods. Generally, image alignment can be divided into three levels: global-level, mid-level, and pixel-level alignment. Global-level alignment typically involves estimating a homography matrix, which can be accomplished using unsupervised deep learning frameworks [24, 25]. This technique effectively aligns images under conditions of planar scenes or when the camera undergoes basic rotational or translational motion. Moreover, through global-to-local homog-

raphy flow refinement, it can be naturally extended to local mesh-grid homography estimation, allowing it to overcome the limitations of a single homography [24]. However, global- and mid-level methods are restricted in their ability to address more complex scenarios, like parallax, non-rigid deformations, or significant foreground motion, since they assume single or multiple global transformations across the entire image.

Another prominent technique involves the pixel-level approaches with optical flow and image warping [2, 11, 49, 63]. Despite progress in image alignment, current optical flow-based methods face challenges that limit their effectiveness in practical applications. A major issue is the sensitivity of optical flow methods to brightness changes. Variations in lighting conditions, such as shadows, reflections, or changes in ambient light, can significantly distort the brightness constancy assumption, leading to incorrect motion estimation. Besides, the warping process inherent in optical flow-based alignment can introduce various artifacts. Inaccuracies in the motion field can lead to distortions such as stretching, compressing, or tearing of image regions. Additionally, the many-to-one mapping inherent in image warping on occlusion regions inevitably results in ghosting artifacts, as depicted in Fig. 1 (a), even with precise optical flow estimation. Such artifacts not only degrade the visual quality of the aligned frames but also affect the accuracy of subsequent processing tasks.

In this paper, we introduce DMAligner, a diffusion-based framework for image alignment through alignment-oriented view synthesis. As depicted in Fig. 2, the desired image alignment result represents a scenario where the camera pose stays fixed at P_1 while time advances from t_1 to t_2 . DMAligner is designed to handle the challenges in image alignment from a new perspective with a generation-based solution (see Fig. 1 (b)), exhibiting strong capabilities and avoiding issues associated with homography and flow-based image warping. Specifically, we first create Dynamic Scene Image Alignment (DSIA) dataset, designed to simulate typical image alignment challenges including camera shifts, moving objects, and fluctuating illumination. Moreover, we propose the Dynamics-aware Diffusion Training approach on the Latent Diffusion Model [38] for learning conditional image generation. The key idea is to enhance the network’s capacity to recognize dynamic information during diffusion model training. This is realized through the Dynamics-aware Mask Producing (DMP) module, which effectively discriminates dynamic foreground regions from static backgrounds within the hidden features across frames. Additionally, we validate the effectiveness of DMAligner through extensive testing on synthetic datasets, including the proposed DSIA and Sintel [3], as well as on the widely-used real-world dataset DAVIS [4]. Both the quantitative and qualitative results demonstrate significant

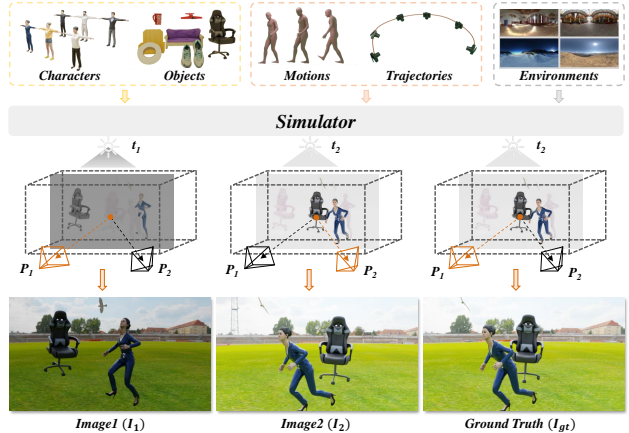


Figure 2. Overview of DSIA dataset generation. The ground truth image is rendered by setting the time to t_2 and the camera pose to P_1 , where the background statics mirror those in I_1 , and the dynamics are akin to I_2 , with slight visualization variances caused by pose changes. As a result, I_{gt} can be regarded as the *alignment-oriented view synthesis* with reference from I_2 to I_1 (i.e., I_2' for I_2 to I_1 alignment).

enhancements over contemporary methods. The contributions are summarized as follows:

- We develop **DSIA** dataset, the first large-scale dataset specific for image alignment, which simulates the typical challenges including camera motion, moving objects, and changes in illumination.
- We present **DMAligner**, a novel diffusion-based framework for image alignment via alignment-oriented view synthesis. The central idea is to enhance the network’s capability to capture dynamic information during diffusion model training, with the assistance of our **DMP** module.
- The proposed method achieves **state-of-the-art performance** on DSIA benchmarks and also demonstrates the **superior generalization capability** on both synthetic and real-world datasets.

2. Related Work

Image Alignment. Traditional approaches primarily rely on feature-based methods, where keypoints are detected and matched across images, followed by geometric transformation estimation to align the images [22, 62]. In the deep learning era, DCNNs [68] have revolutionized image alignment in feature space, which is widely applied in video super-resolution [46], video denoising [61], and burst image restoration [10]. In image space, Global- and middle-level alignments typically involve estimating a homography matrix [25] and local mesh-grid homography [24], respectively. But they cannot handle complex scenarios, involving parallax, non-rigid deformations, or significant foreground motion. A notable advancement in image align-

ment is the adoption of optical flow-based image warping techniques. Optical flow calculates pixel-wise motion between consecutive images, enabling the warping of one image to align with another. With the advances of recent optical flow approaches [7, 28, 31, 36, 41], this method has found widespread use across a variety of video-based applications [1, 2, 11, 27, 55, 63]. Despite their success, warping in occlusion regions inevitably leads to ghosting artifacts, even with accurate flow, as shown in Fig. 1. In contrast, our DMAligner addresses the challenges in image alignment from a new perspective, performing *alignment-oriented view synthesis* using a diffusion-based framework.

Diffusion Model. Diffusion models own prominent generative performance for synthesis [14, 56], and various approaches have been developed to improve the performance or efficiency, such as DDPM [14], DDIM [42], LDM [38] and DDNM [50] etc. Different applications have shown good performances when empowered with diffusion models, including but not limited to, optical flow estimation [29, 39], shadow removal [30], image rectangling [67], homography estimation [20], rolling shutter removal [57], low-light image enhancement [15, 16] and camouflaged object detection [65]. In this work, we propose an end-to-end diffusion-based framework that *specifically handles cross-frame dynamic information* for image alignment.

3. Method

3.1. DSIA Dataset Generation

To the best of our knowledge, *there is no large-scale dataset that addresses the specific challenges of image alignment, such as camera motion, moving objects, and varying illumination, while also providing corresponding ground truth images.* To fill this gap, we create the Dynamic Scene Image Alignment (DSIA) dataset, which simulates these challenges and includes 1,033 indoor and outdoor scenes with over 30K image pairs at a resolution of 960×540 . The main idea is to *simulate the burst image capturing processes with the moving camera across a variety of dynamic scenes.* Fig. 2 illustrates the overview of DSIA dataset generation.

Specifically, inspired by PointOdyssey [66] and Kubric [13], we assemble 25 characters and 100 objects with diverse shapes and materials from several open-source sources, including BlenderKit, Mixamo, GSO [9], and PartNet [35]. These characters are animated using real-world motion capture data [34], while the locations and rotations of object poses are randomly adjusted to simulate realistic motion [13]. Camera motion is controlled along predefined trajectories extracted from [21]. By collecting and animating these assets (characters, objects, and cameras), we generate 3D virtual scenes that closely mimic real-world dynamics. These scenes are then rendered with the Blender

engine, producing image sequences $\{I_1, I_2, \dots, I_N\}$, in which characters, objects, and the camera all move simultaneously. To maximize the diversity of the generated images, we randomly introduce HDR environments with various materials, textures, and lighting conditions, similar to those in [48].

We systematically rearrange the sequencing of the camera trajectories relative to character and object motions, capturing dynamic scenes from various positions along the trajectories, and rendering to generate virtual viewpoint images tailored for image alignment. Considering two consecutive images, I_1 and I_2 involve both global camera motion \mathcal{H} and local foreground movement \mathcal{F} . Their transformations can be described using the traditional warp operation \mathcal{W} :

$$I_1 = \mathcal{W}(I_2) + \mathcal{T} = \mathcal{H}(\mathcal{F}(I_2)) + \mathcal{T}, \quad (1)$$

where \mathcal{T} represents the changes in image texture. In our approach, we capture the dynamic scene at the time of I_2 from the camera viewpoint of I_1 , generating the aligned image I_{gt} as Ground Truth. Compared to I_1 , I_{gt} involves local foreground movement \mathcal{F} , while compared to I_2 , I_{gt} involves global camera motion \mathcal{H} :

$$I_{gt} = \mathcal{H}(I_2) = \mathcal{F}(I_1) + \mathcal{T}. \quad (2)$$

The dataset is divided into four subsets based on varying camera and foreground movements.

3.2. Diffusion Model for Image Alignment

3.2.1. Overview.

The training and inference pipelines of our DMAligner are depicted in Fig. 3. The entire process is formulated in the latent space using LDM[38]. The core insight is to equip the network with the ability to capture dynamic information during diffusion model training. This is accomplished by the Dynamics-aware Mask Producing (DMP) module, which effectively differentiates dynamic foreground regions from static backgrounds within the cross-frame hidden features. We elaborate on the model training and inference details in the following subsections.

3.2.2. Dynamics-aware Diffusion Training.

Given a set of image data I_1 , I_2 , and I_{gt} , we follow LDM [38] to transform these high-resolution images into the latent representational space using a perceptual compression model based on the encoder-decoder architecture, and then reconstruct them back into RGB images. Specifically, for I_{gt} , the encoder \mathcal{E} encodes it into the latent representation V_{gt} , and the decoder \mathcal{D} reconstructs it into the RGB image:

$$\tilde{I}_{gt} = \mathcal{D}(V_{gt}) = \mathcal{D}(\mathcal{E}(I_{gt})). \quad (3)$$

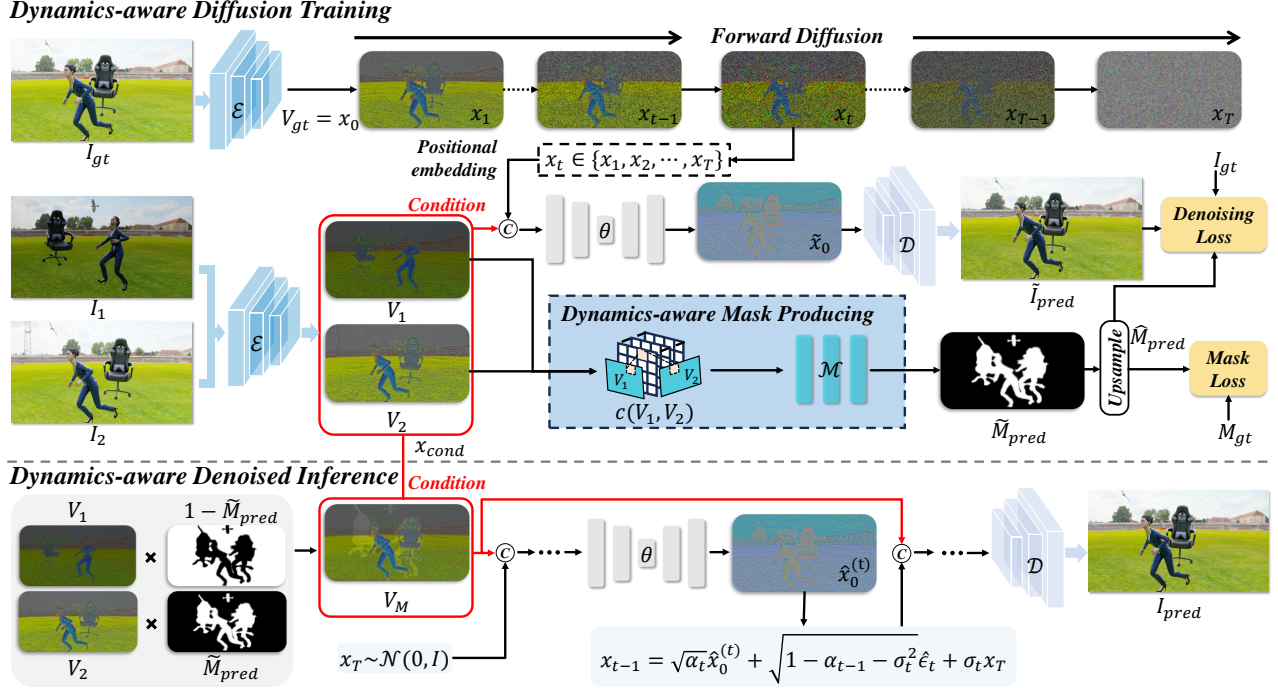


Figure 3. Overview of our DMLAligner. Instead of using the discriminative learning paradigm for optical flow estimation and image warping, our framework employs a generative approach to achieve image alignment with a diffusion model. Dynamics-aware Mask Producing (DMP) module is crucial for providing dynamic information, essential for performing the Dynamics-aware Diffusion Training process in this task.

The same process is applied to I_1 and I_2 , resulting in latent representations V_1 and V_2 . We use V_1 and V_2 as the condition in the latent representational space and train the diffusion model θ to learn sampling from standard Gaussian noise, generating the latent that matches the distribution of V_{gt} . Our training scheme consists of four components: Forward Diffusion, Conditional Learning, Dynamics-aware Mask Producing, and Loss Function.

Forward Diffusion: As illustrated in Fig. 3, we apply different timesteps t to add varying levels of noise to V_{gt} (denoted as x_0), generating a series of noise representations $x_t \in \{x_1, x_2, \dots, x_T\}$. x_t indicates any noise representation at a specific timestep t , and as t increases, the level of added noise grows, leading to an increase in the entropy of the distribution of x_t . Ultimately, the distribution becomes standard Gaussian noise, $x_T \sim \mathcal{N}(0, 1)$, defined as:

$$x_t \in \{x_1, x_2, \dots, x_T\}, x_T \sim \mathcal{N}(0, 1), x_0 = V_{gt}. \quad (4)$$

The forward diffusion process typically follows the approach of [14], where Gaussian noise is incrementally added to the data sample based on a Markov chain. This allows for the diffusion from x_0 to any timestep x_t in one step using the following equation:

$$q(x_t | x_0) = \mathcal{N}(x_t | \sqrt{\bar{\alpha}_t}x_0, (1 - \bar{\alpha}_t)I), \quad (5)$$

where $\bar{\alpha}_t$ represents the cumulative product of a set of pre-

defined noise variance schedules $\{\beta_1, \beta_2, \dots, \beta_t\}$, which ensures that the noise incrementally increases with t , defined as $\bar{\alpha}_t := \prod_{i=1}^t \alpha_i = \prod_{i=1}^t (1 - \beta_i)$.

Dynamics-aware Mask Producing: Notably, our approach explicitly leverages the motion foreground mask to guide the network θ in learning denoising process. This guidance makes the network focus on the moving foreground objects, enabling the better reconstruction of aligned images with enhanced local details. The model relies on our DMP to generate motion foreground masks during training. Specifically, we first compute the correlation $\mathcal{C}(V_1, V_2)$ between V_1 and V_2 to extract sufficient motion information, then input $\mathcal{C}(V_1, V_2)$ into the mask predictor \mathcal{M} to derive the predicted mask \tilde{M}_{pred} , as shown in Eq. 6:

$$\begin{aligned} \mathcal{C}(V_1, V_2) &= \sum_{o \in \Theta} \langle V_1(u), V_2(u+o) \rangle, \\ \tilde{M}_{pred} &= \mathcal{M}(\mathcal{C}(V_1, V_2)), \end{aligned} \quad (6)$$

where u represents the spatial coordinates of V_1 , Θ denotes the neighborhood of coordinate u , and o is the coordinate offset. Importantly, when using the foreground mask to guide the denoising process, we also aim to ensure that network notices the transition regions between foreground and background. To achieve smooth transitions at the edges of foreground objects, we apply the dilation operation d_r to

Table 1. Comparison of network inputs among DPFlow [36], COGS [17], GenWarp [40], and our DMAligner. Other optical flow networks (PWCNet [43], RAFT [44], FlowFormer++ [41], FlowDiffuser [29]) have the same input structure as DPFlow.

Method	Main Input Structure
DPFlow [36]	2 images (I_1, I_2)
COGS [17]	2 images (I_1, I_2) + Depth (D_1, D_2) + Mask (M_1, M_2)
GenWarp [40]	Single image (I_2) + Camera Intrinsics (K) + Depth (D_2) + Camera Motion ($P_{I_2 \rightarrow I_1}$)
DMAligner	2 images (I_1, I_2)

expand the produced mask r times.

$$V_M = V_2 \times d_r(\tilde{M}_{pred}) + V_1 \times \{1 - d_r(\tilde{M}_{pred})\}, \quad (7)$$

as shown in Eq. 7, the expanded foreground mask $d_r(\tilde{M}_{pred})$ is used to fuse the background of V_1 with the foreground of V_2 , creating the mixed latent representation V_M , which serves as a condition to guide the diffusion network in generating the aligned image output.

Conditional Learning: As shown in Fig. 3, we concatenate V_1 , V_2 and V_M along the channel dimension to form the condition x_{cond} , then randomly select x_t from the noise representations $\{x_1, x_2, \dots, x_T\}$, allowing the diffusion model θ to learn the denoising process. This enables θ to handle any x_t at an arbitrary timestep t , producing a denoised output \hat{x}_0 . Similar to approaches in [18, 29, 45], we use the ‘‘predict x_0 ’’ denoising setting in our model. The condition x_{cond} is concatenated with x_t and the encoded timestep t through positional embedding (PE) [47], and the result input is sent to the diffusion model to obtain the denoised result \tilde{x}_0 :

$$\tilde{x}_0 = \theta([x_t, x_{cond}, \text{PE}(t)]), \quad (8)$$

then \tilde{x}_0 is reconstructed to become \tilde{I}_{pred} by decoder \mathcal{D} , which can be expressed as $\tilde{I}_{pred} = \mathcal{D}(\tilde{x}_0)$. Experiments demonstrate that ‘‘predict x_0 ’’ is more effective for image alignment compared to others.

Loss Function: Our model directly learns to denoise and reconstruct a latent representation \tilde{x}_0 from x_t that matches the distribution of V_{gt} . Then, it is decoded by \mathcal{D} into the RGB image \tilde{I}_{pred} , supervised by I_{gt} in the image domain to ensure reliable and accurate output. Additionally, the trainer learns the motion foreground mask \tilde{M}_{pred} , which is then upsampled to obtain \hat{M}_{pred} , helping the model to focus on regions with significant variance. The denoising loss function, namely Denoising Loss, is defined as follows:

$$\hat{M}_{pred} = \text{Upsample}\{d_r(\tilde{M}_{pred})\}, \quad (9)$$

$$L_{\text{Denoising}} = (1 - \gamma) \left\| (1 - \hat{M}_{pred})(I_{gt} - I_{pred}) \right\|_2 + \gamma \left\| (\hat{M}_{pred})(I_{gt} - I_{pred}) \right\|_2, \quad (10)$$

where γ is a variable weighting coefficient, and d_r represents the dilation operation applied to the mask r times. We also supervise the mask \tilde{M}_{pred} using the cross-entropy loss, called as Mask Loss:

$$L_{\text{Mask}} = -M_{gt} \log(\hat{M}_{pred}) - (1 - M_{gt}) \log(1 - \hat{M}_{pred}). \quad (11)$$

The total loss is:

$$L_{\text{Total}} = \lambda_1 L_{\text{Denoising}} + \lambda_2 L_{\text{Mask}}. \quad (12)$$

In our experiments, the parameters r (in d_r), λ_1 , and λ_2 are set to 2, 2, and 0.1, respectively.

3.2.3. Dynamics-aware Denoised Inference.

After training, the diffusion model θ performs inference by denoising a standard Gaussian noise $x_T \in \mathcal{N}(0, 1)$, conditioned on V_1 , V_2 and V_M . This process reconstructs a reliable and accurate alignment result through recurrent denoising. Specifically, the model θ takes x_T , the condition, and the timestep T as inputs according to Eq. 8, producing an initial coarse denoised output $\hat{x}_0^{(T)}$. Then, following the non-Markovian forward process [42] parametrized by σ as shown in Eq. 13, it generates x_{T-1} at timestep $T - 1$. This process is repeated recurrently, producing a sequence of progressively refined denoised results $\hat{x}_0^{(T)}, \hat{x}_0^{(T-1)}, \dots, \hat{x}_0^{(1)}$. Finally, $\hat{x}_0^{(1)}$ is passed through the decoder \mathcal{D} to output the aligned image I_{pred} . The non-Markovian forward process is defined as:

$$x_{t-1} = \sqrt{\alpha_{t-1}} \hat{x}_0^{(t)} + \sqrt{1 - \alpha_{t-1} - \sigma_t^2} \hat{\epsilon}_t + \sigma_t x_T, \quad (13)$$

where $\hat{x}_0^{(t)}$ is the prediction of x_0 from x_t using the diffusion model θ , and $\hat{\epsilon}_t$ is the approximate noise calculated by

$$\hat{\epsilon}_t = \frac{x_t - \sqrt{\alpha_t} \hat{x}_0^{(t)}}{\sqrt{1 - \alpha_t}}. \quad (14)$$

In the recurrent update process described above, the step size Δ is not fixed and can be adjusted to other values. By setting an appropriate step size Δ , inference can be accelerated while still allowing incremental refinement of the results. The iterative update process can be expressed as: $\{x_T \rightarrow \hat{x}_0^{(T)}\} \rightarrow \{x_{T-\Delta} \rightarrow \hat{x}_0^{(T-\Delta)}\} \rightarrow \dots \rightarrow \{x_1 \rightarrow \hat{x}_0^{(1)}\}$. In our empirical analysis, we set $T = 1000$ and $\Delta = 20$.

4. Experiments

4.1. Input Structure

As shown in Tab. 1, the input requirements for DPFlow [36], COGS [17], GenWarp [40], and our DMAligner are explained. Both DPFlow and DMAligner only require two

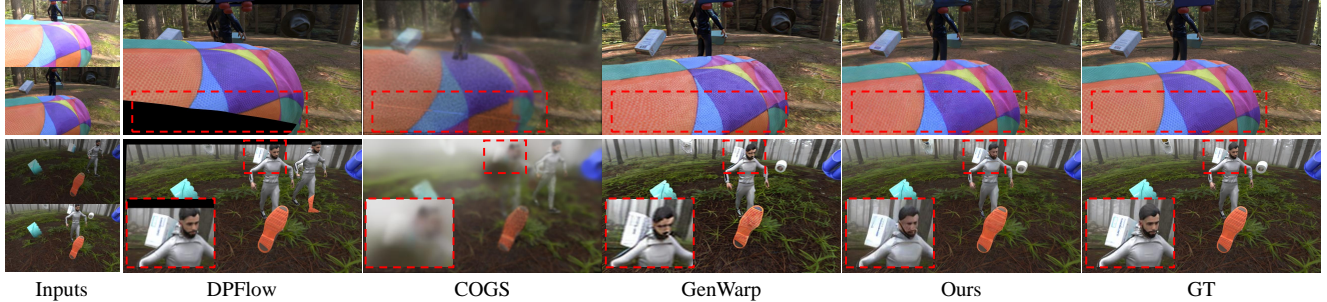


Figure 4. Qualitative comparisons between DPFlow [36], COGS [17], GenWarp [40] and our DMAligner on our DSIA dataset.

Table 2. Quantitative comparison on our DSIA dataset across four subsets (LcLf, LcSf, ScLf, and ScSf) using PSNR and SSIM metrics, *higher scores indicate better performance*. The average (“Avg”) across all subsets summarizes overall results. † indicates that occlusion and ghost regions are excluded during metric computation, as determined by forward-backward consistency check [54].

Methods	LcLf		LcSf		ScLf		ScSf		Avg.	
	PSNR↑	SSIM↑								
<i>Methods based on Flow Warping</i>										
PWCNet [43]	16.53	0.74	16.40	0.73	20.53	0.74	21.01	0.76	18.62	0.74
RAFT [44]	18.22	0.74	18.34	0.74	22.46	0.77	22.95	0.76	20.49	0.75
FlowFormer++ [41]	21.02	0.75	20.97	0.76	22.84	0.77	23.94	0.79	22.19	0.77
FlowDiffuser [29]	20.18	0.75	20.33	0.75	23.39	0.78	23.91	0.79	21.95	0.77
DPFlow [36]	20.78	0.76	20.50	0.74	23.94	0.78	24.61	0.80	22.46	0.77
PWCNet† [43]	22.03	0.76	21.15	0.76	24.63	0.79	24.74	0.77	23.14	0.77
RAFT† [44]	22.99	0.78	23.15	0.77	25.07	0.80	25.09	0.79	24.08	0.78
FlowFormer++† [41]	24.19	0.79	24.24	0.78	25.61	0.81	25.74	0.81	24.95	0.80
FlowDiffuser† [29]	23.82	0.78	23.81	0.77	25.78	0.81	25.89	0.82	24.82	0.80
DPFlow† [36]	<u>24.30</u>	<u>0.79</u>	<u>24.84</u>	<u>0.79</u>	<u>25.99</u>	0.82	<u>26.04</u>	<u>0.82</u>	<u>25.29</u>	<u>0.81</u>
<i>Methods based on View Synthesis</i>										
COGS [17]	16.35	0.66	16.84	0.69	17.01	0.69	18.21	0.71	17.10	0.69
SD-Inpaint [59]	22.14	0.75	22.92	0.76	25.42	0.79	25.77	0.81	24.06	0.78
GenWarp [40]	22.62	0.76	23.15	0.76	25.32	0.78	25.84	0.81	24.23	0.78
DMAligner(Ours)	24.91	0.80	26.90	0.81	27.25	<u>0.81</u>	27.64	0.83	26.67	0.81

consecutive image frames I_1 and I_2 for optical flow estimation and view synthesis, respectively. On the other hand, COGS relies on Gaussian splatting and requires not only the two input images I_1 and I_2 , but also foreground masks (M_1, M_2) and depth maps (D_1, D_2), with the masks predicted by FC-CLIP [60] and depth estimated by Marigold [19]. These additional inputs are crucial for its 3D scene reconstruction. Although GenWarp is described as using only a single image I_2 as input, it actually relies on both I_1 and I_2 to obtain the relative camera motion $P_{I_2 \rightarrow I_1}$, which can be derived from the optical flow $F_{I_2 \rightarrow I_1}$ estimated by DPFlow, filtering out local motion to capture the overall camera movement [23, 32, 33]. Besides, it also needs camera intrinsics (K), depth (D_2) from Marigold. Therefore, GenWarp also relies on information from both I_1 and I_2 . Unlike GenWarp and COGS, our DMAligner does not require additional geometric information such as camera intrinsics, depth maps, or pose transformations, making it a simpler and more direct approach for alignment.

4.2. Implementation Details

Our DSIA dataset comprises 1,033 indoor and outdoor scenes with a resolution of 960×540 . The dataset is divided into a training set with over 30k samples and a test set with 2k samples. We partition the test set into four subsets based on the magnitude of camera and foreground motion: LcLf, LcSf, LcSf and ScSf (Lc: large camera motion, Lf: large foreground motion, Sc: small camera motion, Sf: small foreground motion). Following LDM [38], we train DMAligner use the VQ-VAE with pretrained weights, freeze it after fine-tuning, and train denoising UNet. Training uses random 480×256 crops with flipping, while inference supports larger inputs on a single GPU.

4.3. Comparison with Existing Methods

4.3.1. Results on DSIA.

Tab. 2 compares our DMAligner with some flow-warping methods and view-synthesis methods. In our DSIA dataset, all flow-warping methods are trained using rendered ground



Figure 5. Qualitative comparisons between DPFlow [36], GenWarp [40] and our DMAligner on Sintel dataset.



Figure 6. Qualitative comparisons between DPFlow [36], GenWarp [40] and our DMAligner on the real-world DAVIS dataset.

truth optical flow. We then align I_2 to I_{gt} using back warping and compute PSNR and SSIM between I_{pred} and I_{gt} . To address occlusion and ghosting artifacts from warping, these regions (determined by forward-backward consistency check [54]) are excluded from the metrics calculation, as marked by \dagger . Fig. 4 shows qualitative visual results on the DSIA test set, our DMAligner most closely matches the ground truth.

4.3.2. Results on Sintel and DAVIS.

We conduct qualitative comparisons on and the synthetic Sintel [3] dataset and the realistic DAVIS [4] dataset to evaluate the cross-domain performance of DMAligner and DSIA dataset. All competing methods and our DMAligner are trained on DSIA, and alignment results are directly tested on the Sintel Clean, Sintel Final training sets, and the DAVIS dataset. As there is no ground truth for precise evaluation, we calculate the feature distances between I_{pred} and I_1 using LPIPS [64] and DreamSim [12]. Tab. 3

presents the quantitative results on Sintel and DAVIS, where DMAligner achieves the best average LPIPS and DreamSim scores. Fig. 6 shows examples from the DAVIS dataset, and Fig. 5 displays results from the Sintel test set. These results demonstrate that DMAligner delivers exceptional image alignment performance in both synthetic and real-world scenarios.

4.3.3. Results on Downstream HDR Task.

In HDR imaging [53], LDR frames with alternating exposures (e.g., L_{t-1}, L_t, L_{t+1}) are aligned using flow warping before fusion. We replace this step with DMAligner, which aligns foreground and background more robustly, generating warped frames ($L_{t+1 \rightarrow t}, L_{t-1 \rightarrow t}$). Importantly, the fusion network and overall pipeline remain unchanged—only the aligned inputs differ. In Fig. 7, our method produces fewer artifacts, demonstrating strong generalization with existing HDR fusion network, which is expected to improve other downstream tasks as well.

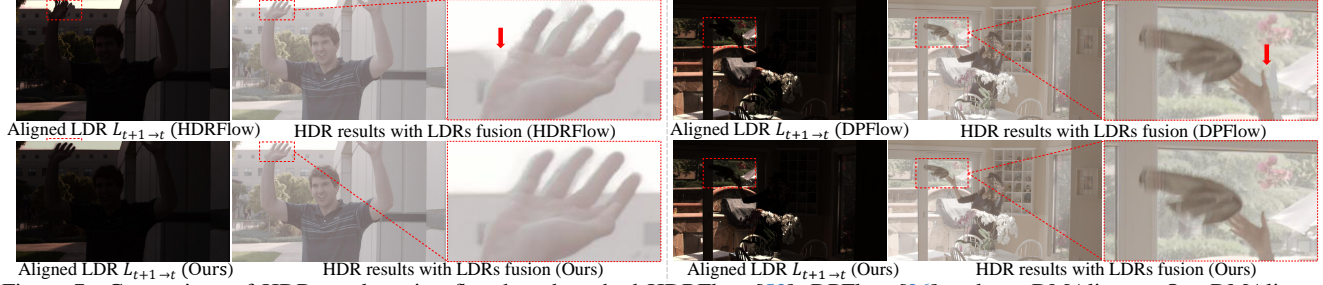


Figure 7. Comparison of HDR results using flow-based method HDRFlow [53], DPFlow [36] and our DMAligner. Our DMAligner significantly reduces ghosting and background distortions, especially around occluded regions and moving objects.

Table 3. Quantitative comparison on Sintel and DAVIS dataset. Due to the lack of ground truth for precise evaluation, we compute LPIPS [64] and DreamSim [12] between I_{pred} and I_1 . Lower scores indicate better performance.

Methods	Sintel (Clean)		Sintel (Final)		DAVIS		Avg.	
	LPIPS↓	DreamSim↓	LPIPS↓	DreamSim↓	LPIPS↓	DreamSim↓	LPIPS↓	DreamSim↓
<i>Methods based on Flow Warping</i>								
PWCNet [43]	0.251	0.146	<u>0.177</u>	0.109	0.217	0.102	0.215	0.119
RAFT [44]	0.245	0.141	0.171	<u>0.102</u>	0.219	0.104	<u>0.212</u>	0.116
FlowFormer++ [41]	0.264	0.150	0.184	0.113	0.224	0.106	0.224	0.123
FlowDiffuser [29]	0.258	0.141	0.179	0.103	0.211	0.090	0.216	0.111
DPFlow [36]	0.255	<u>0.138</u>	0.178	0.101	<u>0.209</u>	<u>0.087</u>	0.214	<u>0.109</u>
<i>Methods based on View Synthesis</i>								
COGS [17]	0.411	0.172	0.378	0.131	0.398	0.121	0.396	0.142
SD-Inpaint [59]	0.269	0.164	0.271	0.142	0.241	0.114	0.260	0.140
GenWarp [40]	0.264	0.152	0.251	0.130	0.234	0.108	0.250	0.130
DMAligner(Ours)	<u>0.246</u>	0.123	0.186	0.117	0.202	0.084	0.211	0.108

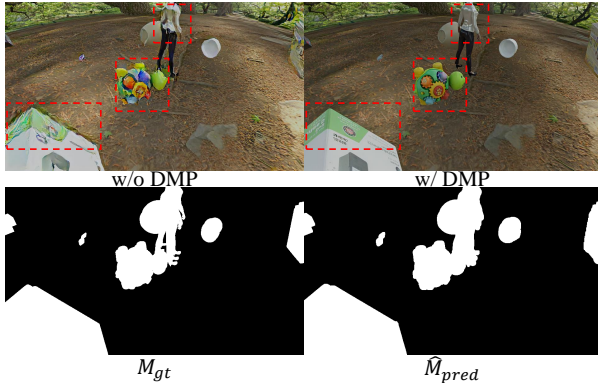


Figure 8. Ablation experiments of DMP. The results of DMAligner without or with DMP are given, as well as the mask prediction \hat{M}_{pred} and mask labels M_{gt} .

4.4. Ablation Study

In Tab. 4, we explore the impact of predict methods and DMP. Comparing (a)&(b) and (c)&(d)&(e), “predict x_0 ” is more effective for image alignment, as it directly targets image reconstruction. comparing (b)&(e), DMP results in more accurate alignment, as it allows the model to better focus on relevant areas. Fig. 8 also demonstrates that DMP enables the network to focus on the local dynamic foreground areas, improving the foreground details of the generated aligned images and achieving superior alignment.

Table 4. Ablation studies of predict methods and our DMP.

Exp.	Predict Methods	DMP	Avg	
			PSNR	SSIM
(a)	pred \hat{e}_t	w/o	24.82	0.77
(b)	pred x_0	w/o	25.12	0.79
(c)	rectified flow	w/	25.98	0.80
(d)	v-prediction	w/	26.16	0.81
(e)	pred x_0	w/	26.67	0.81

5. Conclusion

This work represents a significant paradigm shift in image alignment by introducing a generation-based solution. The proposed DMAligner framework, a diffusion-based approach for image alignment through alignment-oriented view synthesis, effectively addresses challenges such as ghosting artifacts, occlusions, and illumination changes that previous methods struggle with. Notably, a Dynamics-aware Mask Producing (DMP) module is introduced to enable the diffusion model to better handle dynamic foreground regions that are prone to errors. Additionally, the Dynamic Scene Image Alignment (DSIA) dataset is developed specifically for training. Extensive experiments demonstrate that DMAligner outperforms previous methods with unmatched performance and exhibits strong cross-domain capabilities, excelling in both synthetic and real-world scenarios.

References

- [1] Goutam Bhat, Martin Danelljan, Luc Van Gool, and Radu Timofte. Deep burst super-resolution. In *Proc. CVPR*, pages 9209–9218, 2021. 3
- [2] Goutam Bhat, Martin Danelljan, Fisher Yu, Luc Van Gool, and Radu Timofte. Deep reparametrization of multi-frame super-resolution and denoising. In *Proc. ICCV*, pages 2460–2470, 2021. 2, 3
- [3] Daniel J Butler, Jonas Wulff, Garrett B Stanley, and Michael J Black. A naturalistic open source movie for optical flow evaluation. In *Proc. ECCV*, pages 611–625, 2012. 2, 7
- [4] Sergi Caelles, Jordi Pont-Tuset, Federico Perazzi, Alberto Montes, Kevis-Kokitsi Maninis, and Luc Van Gool. The 2019 davis challenge on vos: Unsupervised multi-object segmentation. *arXiv preprint arXiv:1905.00737*, 2019. 2, 7
- [5] Kelvin CK Chan, Xintao Wang, Ke Yu, Chao Dong, and Chen Change Loy. Understanding deformable alignment in video super-resolution. In *Proc. AAAI*, pages 973–981, 2021. 1
- [6] Rufeng Chen, Bolun Zheng, Hua Zhang, Quan Chen, Cheng-gang Yan, Gregory Slabaugh, and Shanxin Yuan. Improving dynamic hdr imaging with fusion transformer. In *Proc. AAAI*, pages 340–349, 2023. 1
- [7] Changxing Deng, Ao Luo, Haibin Huang, Shaodan Ma, Jiangyu Liu, and Shuaicheng Liu. Explicit motion disentangling for efficient optical flow estimation. In *Proc. ICCV*, pages 9521–9530, 2023. 3
- [8] Xuan Dong, Xiaoyan Hu, Weixin Li, Xiaojie Wang, and Yunhong Wang. Miehdr cnn: Main image enhancement based ghost-free high dynamic range imaging using dual-lens systems. In *Proc. AAAI*, pages 1264–1272, 2021. 1
- [9] Laura Downs, Anthony Francis, Nate Koenig, Brandon Kinman, Ryan Hickman, Krista Reymann, Thomas B McHugh, and Vincent Vanhoucke. Google scanned objects: A high-quality dataset of 3d scanned household items. In *Proc. ICRA*, pages 2553–2560, 2022. 3
- [10] Akshay Dudhane, Syed Waqas Zamir, Salman Khan, Fahad Shahbaz Khan, and Ming-Hsuan Yang. Burst image restoration and enhancement. In *Proc. CVPR*, pages 5759–5768, 2022. 2
- [11] Thibaud Ehret, Axel Davy, Jean-Michel Morel, Gabriele Facciolo, and Pablo Arias. Model-blind video denoising via frame-to-frame training. In *Proc. CVPR*, pages 11369–11378, 2019. 2, 3
- [12] Stephanie Fu, Netanel Tamir, Shobhita Sundaram, Lucy Chai, Richard Zhang, Tali Dekel, and Phillip Isola. Dreamsim: Learning new dimensions of human visual similarity using synthetic data. In *Proc. NeurIPS*, pages 50742–50768, 2023. 7, 8
- [13] Klaus Greff, Francois Belletti, Lucas Beyer, Carl Doersch, Yilun Du, Daniel Duckworth, David J Fleet, Dan Gnanaprasgam, Florian Golemo, Charles Herrmann, et al. Kubric: A scalable dataset generator. In *Proc. CVPR*, pages 3749–3761, 2022. 3
- [14] Jonathan Ho, Ajay Jain, and Pieter Abbeel. Denoising diffusion probabilistic models. *Proc. NeurIPS*, 33:6840–6851, 2020. 3, 4
- [15] Hai Jiang, Ao Luo, Haoqiang Fan, Songchen Han, and Shuaicheng Liu. Low-light image enhancement with wavelet-based diffusion models. *ACM Trans. Graphics*, pages 1–14, 2023. 3
- [16] Hai Jiang, Ao Luo, Xiaohong Liu, Songchen Han, and Shuaicheng Liu. Lightendiffusion: Unsupervised low-light image enhancement with latent-retinex diffusion models. In *Proc. ECCV*, 2024. 3
- [17] Kaiwen Jiang, Yang Fu, Mukund Varma T, Yash Belhe, Xiaolong Wang, Hao Su, and Ravi Ramamoorthi. A construct-optimize approach to sparse view synthesis without camera pose. In *Proc. ACM SIGGRAPH*, pages 1–11, 2024. 5, 6, 8
- [18] Tero Karras, Miika Aittala, Timo Aila, and Samuli Laine. Elucidating the design space of diffusion-based generative models. *Proc. NeurIPS*, 35:26565–26577, 2022. 5
- [19] Bingxin Ke, Anton Obukhov, Shengyu Huang, Nando Metzger, Rodrigo Caye Daudt, and Konrad Schindler. Repurposing diffusion-based image generators for monocular depth estimation. In *Proc. CVPR*, pages 9492–9502, 2024. 6
- [20] Haipeng Li, Hai Jiang, Ao Luo, Ping Tan, Haoqiang Fan, Bing Zeng, and Shuaicheng Liu. Dmhom: Learning homography with diffusion models. *ACM Trans. Graphics*, pages 1–16, 2024. 3
- [21] Zhengqi Li, Tali Dekel, Forrester Cole, Richard Tucker, Noah Snavely, Ce Liu, and William T Freeman. Learning the depths of moving people by watching frozen people. In *Proc. CVPR*, pages 4521–4530, 2019. 3
- [22] Ce Liu, Jenny Yuen, and Antonio Torralba. Sift flow: Dense correspondence across scenes and its applications. *IEEE Trans. on Pattern Analysis and Machine Intelligence*, pages 978–994, 2010. 2
- [23] Shuaicheng Liu, Ping Tan, Lu Yuan, Jian Sun, and Bing Zeng. Meshflow: Minimum latency online video stabilization. In *Proc. ECCV*, pages 800–815, 2016. 6
- [24] Shuaicheng Liu, Yuhang Lu, Hai Jiang, Nianjin Ye, Chuan Wang, and Bing Zeng. Unsupervised global and local homography estimation with motion basis learning. *IEEE Trans. on Pattern Analysis and Machine Intelligence*, pages 7885–7899, 2022. 1, 2
- [25] Shuaicheng Liu, Nianjin Ye, Chuan Wang, Jirong Zhang, Lanpeng Jia, Kunming Luo, Jue Wang, and Jian Sun. Content-aware unsupervised deep homography estimation and its extensions. *IEEE Trans. on Pattern Analysis and Machine Intelligence*, pages 2849–2863, 2022. 1, 2
- [26] Shuaicheng Liu, Zhuofan Zhang, Zhen Liu, Ping Tan, and Bing Zeng. Minimum latency deep online video stabilization and its extensions. *IEEE Trans. on Pattern Analysis and Machine Intelligence*, 47(2):1238–1249, 2025. 1
- [27] Zhen Liu, Yinglong Wang, Bing Zeng, and Shuaicheng Liu. Ghost-free high dynamic range imaging with context-aware transformer. In *Proc. ECCV*, pages 344–360, 2022. 3
- [28] Ao Luo, Fan Yang, Xin Li, Lang Nie, Chunyu Lin, Haoqiang Fan, and Shuaicheng Liu. GafLOW: Incorporating gaussian attention into optical flow. In *Proc. ICCV*, pages 9642–9651, 2023. 3

- [29] Ao Luo, Xin Li, Fan Yang, Jiangyu Liu, Haoqiang Fan, and Shuaicheng Liu. Flowdiffuser: Advancing optical flow estimation with diffusion models. In *Proc. CVPR*, pages 19167–19176, 2024. 3, 5, 6, 8
- [30] Jinting Luo, Ru Li, Chengzhi Jiang, Xiaoming Zhang, Mingyan Han, Ting Jiang, Haoqiang Fan, and Shuaicheng Liu. Diff-shadow: Global-guided diffusion model for shadow removal. In *Proc. AAAI*, pages 5856–5864, 2025. 3
- [31] Xinglong Luo, Kunming Luo, Ao Luo, Zhengning Wang, Ping Tan, and Shuaicheng Liu. Learning optical flow from event camera with rendered dataset. In *Proc. ICCV*, pages 9847–9857, 2023. 3
- [32] Xinglong Luo, Ao Luo, Zhengning Wang, Chunyu Lin, Bing Zeng, and Shuaicheng Liu. Efficient meshflow and optical flow estimation from event cameras. In *Proc. CVPR*, pages 19198–19207, 2024. 6
- [33] Xinglong Luo, Ao Luo, Kunming Luo, Zhengning Wang, Ping Tan, Bing Zeng, and Shuaicheng Liu. Learning efficient meshflow and optical flow from event cameras. *IEEE Trans. on Pattern Analysis and Machine Intelligence*, 48(2):1355–1372, 2026. 6
- [34] Naureen Mahmood, Nima Ghorbani, Nikolaus F Troje, Gerard Pons-Moll, and Michael J Black. Amass: Archive of motion capture as surface shapes. In *Proc. ICCV*, pages 5442–5451, 2019. 3
- [35] Kaichun Mo, Shilin Zhu, Angel X Chang, Li Yi, Subarna Tripathi, Leonidas J Guibas, and Hao Su. Partnet: A large-scale benchmark for fine-grained and hierarchical part-level 3d object understanding. In *Proc. CVPR*, pages 909–918, 2019. 3
- [36] Henrique Morimitsu, Xiaobin Zhu, Roberto M. Cesar, Xiangyang Ji, and Xu-Cheng Yin. Dpflow: Adaptive optical flow estimation with a dual-pyramid framework. In *Proc. CVPR*, pages 17810–17820, 2025. 3, 5, 6, 7, 8
- [37] Sicheng Pan and Yingming Li. Ebdnet: Integrating optical flow with kernel prediction for burst denoising. *IEEE Trans. on Circuits and Systems for Video Technology*, 2024. 1
- [38] Robin Rombach, Andreas Blattmann, Dominik Lorenz, Patrick Esser, and Björn Ommer. High-resolution image synthesis with latent diffusion models. In *Proc. CVPR*, pages 10684–10695, 2022. 2, 3, 6
- [39] Saurabh Saxena, Charles Herrmann, Junhwa Hur, Abhishek Kar, Mohammad Norouzi, Deqing Sun, and David J Fleet. The surprising effectiveness of diffusion models for optical flow and monocular depth estimation. In *Proc. NeurIPS*, 2024. 3
- [40] Junyoung Seo, Kazumi Fukuda, Takashi Shibuya, Takuya Narihira, Naoki Murata, Shoukang Hu, Chieh-Hsin Lai, Seungryong Kim, and Yuki Mitsufuji. Genwarp: Single image to novel views with semantic-preserving generative warping. *Proc. NeurIPS*, 37:80220–80243, 2024. 5, 6, 7, 8
- [41] Xiaoyu Shi, Zhaoyang Huang, Dasong Li, Manyuan Zhang, Ka Chun Cheung, Simon See, Hongwei Qin, Jifeng Dai, and Hongsheng Li. Flowformer++: Masked cost volume autoencoding for pretraining optical flow estimation. In *Proc. CVPR*, pages 1599–1610, 2023. 3, 5, 6, 8
- [42] Jiaming Song, Chenlin Meng, and Stefano Ermon. Denoising diffusion implicit models. In *Proc. ICLR*, 2021. 3, 5
- [43] Deqing Sun, Xiaodong Yang, Ming-Yu Liu, and Jan Kautz. Pwc-net: Cnns for optical flow using pyramid, warping, and cost volume. In *Proc. ICCV*, pages 8934–8943, 2018. 5, 6, 8
- [44] Zachary Teed and Jia Deng. Raft: Recurrent all-pairs field transforms for optical flow. In *Proc. ECCV*, pages 402–419, 2020. 5, 6, 8
- [45] Guy Tevet, Sigal Raab, Brian Gordon, Yoni Shafir, Daniel Cohen-or, and Amit Haim Bermano. Human motion diffusion model. In *Proc. ICLR*, 2023. 5
- [46] Yapeng Tian, Yulun Zhang, Yun Fu, and Chenliang Xu. Tdan: Temporally-deformable alignment network for video super-resolution. In *Proc. CVPR*, pages 3360–3369, 2020. 2
- [47] Ashish Vaswani, Noam Shazeer, Niki Parmar, Jakob Uszkoreit, Llion Jones, Aidan N Gomez, Łukasz Kaiser, and Illia Polosukhin. Attention is all you need. In *Proc. NeurIPS*, 2017. 5
- [48] Ye Wang, Norman Mu, Daniele Grandi, Nicolas Savva, and Jacob Steinhardt. A3d: Studying pretrained representations with programmable datasets. In *Proc. CVPR*, pages 4878–4889, 2022. 3
- [49] Yinglong Wang, Zhen Liu, Jianzhuang Liu, Songcen Xu, and Shuaicheng Liu. Low-light image enhancement with illumination-aware gamma correction and complete image modelling network. In *Proc. ICCV*, pages 13128–13137, 2023. 2
- [50] Yinhuai Wang, Jiwen Yu, and Jian Zhang. Zero-shot image restoration using denoising diffusion null-space model. In *Proc. ICLR*, 2023. 3
- [51] Zhengning Wang, Xuhang Liu, Chuan Wang, Ting Jiang, Tianjiao Zeng, Zhenni Zeng, Guoqing Wang, and Shuaicheng Liu. Reconstruction flow recurrent network for compressed video quality enhancement. *Pattern Recognition*, page 110638, 2024. 1
- [52] Liangbin Xie, Xintao Wang, Shuwei Shi, Jinjin Gu, Chao Dong, and Ying Shan. Mitigating artifacts in real-world video super-resolution models. In *Proc. AAAI*, pages 2956–2964, 2023. 1
- [53] Gangwei Xu, Yujin Wang, Jinwei Gu, Tianfan Xue, and Xin Yang. Hdrflow: Real-time hdr video reconstruction with large motions. In *Proc. CVPR*, pages 24851–24860, 2024. 1, 7, 8
- [54] Haofei Xu, Jing Zhang, Jianfei Cai, Hamid Rezafofighi, and Dacheng Tao. Gmflow: Learning optical flow via global matching. In *Proc. CVPR*, pages 8121–8130, 2022. 6, 7
- [55] Tianfan Xue, Baian Chen, Jiajun Wu, Donglai Wei, and William T Freeman. Video enhancement with task-oriented flow. *International Journal of Computer Vision*, pages 1106–1125, 2019. 3
- [56] Ling Yang, Zhilong Zhang, Yang Song, Shenda Hong, Runsheng Xu, Yue Zhao, Wentao Zhang, Bin Cui, and Ming-Hsuan Yang. Diffusion models: A comprehensive survey of methods and applications. *ACM Computing Surveys*, pages 1–39, 2022. 3
- [57] Zhanglei Yang, Haipeng Li, Mingbo Hong, Chen-Lin Zhang, Jiajun Li, and Shuaicheng Liu. Single image rolling shutter

- removal with diffusion models. In *Proc. AAAI*, pages 9373–9381, 2025. 3
- [58] Geunhyuk Youk, Jihyong Oh, and Munchurl Kim. Fmanet: Flow-guided dynamic filtering and iterative feature refinement with multi-attention for joint video super-resolution and deblurring. In *Proc. CVPR*, pages 44–55, 2024. 1
- [59] Jason J Yu, Fereshteh Forghani, Konstantinos G Derpanis, and Marcus A Brubaker. Long-term photometric consistent novel view synthesis with diffusion models. In *Proc. ICCV*, pages 7094–7104, 2023. 6, 8
- [60] Qihang Yu, Ju He, Xueqing Deng, Xiaohui Shen, and Liang-Chieh Chen. Convolutions die hard: Open-vocabulary segmentation with single frozen convolutional clip. *Proc. NeurIPS*, 36:32215–32234, 2023. 6
- [61] Huanjing Yue, Cong Cao, Lei Liao, Ronghe Chu, and Jingyu Yang. Supervised raw video denoising with a benchmark dataset on dynamic scenes. In *Proc. CVPR*, pages 2301–2310, 2020. 2
- [62] Fan Zhang and Feng Liu. Parallax-tolerant image stitching. In *Proc. CVPR*, pages 3262–3269, 2014. 2
- [63] Jiawei Zhang, Jinshan Pan, Daoye Wang, Shangchen Zhou, Xing Wei, Furong Zhao, Jianbo Liu, and Jimmy Ren. Deep dynamic scene deblurring from optical flow. *IEEE Trans. on Circuits and Systems for Video Technology*, pages 8250–8260, 2021. 2, 3
- [64] Richard Zhang, Phillip Isola, Alexei A Efros, Eli Shechtman, and Oliver Wang. The unreasonable effectiveness of deep features as a perceptual metric. In *Proc. CVPR*, pages 586–595, 2018. 7, 8
- [65] Jianwei Zhao, Xin Li, Fan Yang, Qiang Zhai, Ao Luo, Zicheng Jiao, and Hong Cheng. Focusdiffuser: Perceiving local disparities for camouflaged object detection. In *Proc. ECCV*, 2024. 3
- [66] Yang Zheng, Adam W Harley, Bokui Shen, Gordon Wetstein, and Leonidas J Guibas. Pointodyssey: A large-scale synthetic dataset for long-term point tracking. In *Proc. ICCV*, pages 19855–19865, 2023. 3
- [67] Tianhao Zhou, Haipeng Li, Ziyi Wang, Ao Luo, Chen-Lin Zhang, Jiajun Li, Bing Zeng, and Shuaicheng Liu. Recdiffusion: Rectangling for image stitching with diffusion models. In *Proc. CVPR*, pages 2692–2701, 2024. 3
- [68] Xizhou Zhu, Han Hu, Stephen Lin, and Jifeng Dai. Deformable convnets v2: More deformable, better results. In *Proc. CVPR*, pages 9308–9316, 2019. 2